Available online at www.sciencedirect.com
ScienceDirect
Journal of Power Sources 179 (2008) 673–682
JOURNAL OF POWER SOURCES
www.elsevier.com/locate/jpowsour

Nonlinear identification of a DIR-SOFC stack using wavelet networks

Jun Li [a,*], Ying-Wei Kang [a], Guang-Yi Cao [a], Xin-Jian Zhu [a], Heng-Yong Tu [a], Jian Li [b]

[a] *Institute of Fuel Cell, Department of Automation, Shanghai Jiao Tong University, Shanghai 200240, China*
[b] *College of Materials Science and Engineering, Huazhong University of Science and Technology, Wuhan 430074, China*

Received 29 November 2007; received in revised form 7 January 2008; accepted 7 January 2008
Available online 16 January 2008

Abstract

Application of wavelet networks for identification of a direct internal reforming solid oxide fuel cell (DIR-SOFC) stack is reported in this paper. The SOFC is a complex system particularly when it is directly fueled with hydrocarbons (natural gas, coal gas, etc.). Most of the traditional models of the SOFC, based on the reforming, electrochemical and thermal modeling, are too complicated. To facilitate controller design and analysis of systems, the wavelet network dynamic model of the DIR-SOFC is constructed, avoiding the consideration of the complex processes in the fuel cells. The input and output data are used for initializing and training the wavelet network by a recursive approach. The Gram–Schmidt algorithm, the Cross-Validation method and immune selection principles are applied to optimization of the network. The simulation is performed and comparisons of characteristics under different operating conditions are given. The results show high static and dynamic accuracy of the identified model. Further, the obtained wavelet network model can be used for developing the model-based controllers of DIR-SOFC.

Keywords: Direct internal reforming solid oxide fuel cell; Wavelet network; Nonlinear identification; Modeling

1. Introduction

The solid oxide fuel cell (SOFC) is based on a solid-state ion-conducting electrolyte, which functions at high temperature. Due to high efficiency, high reliability, and low levels of noise and pollution, the SOFC has been considered as one of the most promising technologies for electrical energy generation [1]. The high operating temperature (up to 1000 °C) allows internal reforming and promotes rapid kinetics with nonprecious materials. Therefore, the SOFC can be directly fueled with pure hydrogen, natural gas and other hydrocarbons [1,2].

Due to a lot of coupling parameters, the SOFC is considered a complicated nonlinear multi-input and multi-output (MIMO) system which is difficult to model. In the past couple of years, several models [3–10] have been developed and tested to study characteristics of the SOFC stack. Achenbach presented a mathematical model of a planar SOFC and showed the distributions of the current density and temperature obtained by computational method [3]. Further, the dynamic voltage response to an electrical current change was also discussed. Costamagna and Honegger [4] presented and validated a simulation model for a SOFC stack integrated with an air pre-heater. Recknagle et al. [8] developed three-dimensional thermo-fluid electrochemical models of planar SOFC stacks. With the aid of a simulation tool combining a computational fluid dynamics (CFD) code and an electrochemistry calculation method, the distributions of the temperature, current density and fuel species were shown and investigated. In Refs. [9,10], a one-dimensional model has been used for simulation of an anode-supported intermediate temperature DIR-SOFC stack. Further, using this model, the one-dimensional steady-state parameter distribution and dynamic responses to several current density step-changes were generated and discussed. Most of the models are based on the fundamentals of heat, momentum and mass transfer, and are focused on explaining the operation mechanism of the SOFC. Although the models describe the physical and chemical processes well, most of them are too complicated to be applied to controller design.

To simplify the fuel cell models for the performance analysis and valid control strategy design, statistical identification methods based on measurements have gained attention during the recent years [11–13]. Arriagada et al. [11] developed an artificial neural network (ANN) model of SOFC that is applicable to the prediction of the static current density–voltage characteristics

* Corresponding author. Tel.: +86 21 34206249; fax: +86 21 34206249.
E-mail addresses: jun.li.fc@gmail.com, jli@sjtu.org (J. Li).

0378-7753/$ – see front matter © 2008 Elsevier B.V. All rights reserved.
doi:10.1016/j.jpowsour.2008.01.013

Nomenclature

a	dilation parameter of wavelet
A_1, A_2	anodic and cathodic reaction surfaces
b	translation parameter of wavelet
B	stoichiometric matrix
C_p	specific heat capacity ($J\,kg^{-1}\,K^{-1}$)
E	Nernst voltage (V)
E_0	EMF (electro-motive-force) at standard pressure
E_{act}	activation energy ($J\,mol^{-1}$)
F	gas flow rate ($kg\,s^{-1}$)
$\vec{F}$	gas flow rate vector
F_{Far}	Faraday constant ($96{,}485\,C\,mol^{-1}$)
h	gas enthalpy ($J\,kg^{-1}$)
ΔH	enthalpy change ($J\,mol^{-1}$)
I	current density ($A\,m^{-2}$)
I_0	exchange current density ($A\,m^{-2}$)
I_L	limiting current density ($A\,m^{-2}$)
I_m	mean current density ($A\,m^{-2}$)
k_n	rate coefficient for reforming reaction
K_n	equilibrium constant
K^{ad}	adsorption constant
N_w	number of multi-dimensional wavelets
P	partial pressure (bar)
q	heat generation ($J\,m^{-2}\,s^{-1}$)
r	reaction rate ($mol\,m^{-2}\,s^{-1}$)
$\vec{r}$	reaction rate vector
R	gas constant ($8.314\,J\,K^{-1}\,mol^{-1}$)
S_h	heat source ($J\,m^{-3}\,s^{-1}$)
T	temperature (K)
T_{in}	inlet temperature (K)
T_{out}	outlet temperature (K)
$\vec{V}$	gas velocity vector
V_{cell}	cell voltage (V)
V_{out}	stack output voltage (V)
w	coefficient of wavelet
$\vec{W}$	molar mass vector

Greek symbols

α^{an}, α^{ca}	charge transfer coefficients
γ^{an}, γ^{ca}	coefficients for I_0^{an} and I_0^{ca} ($A\,m^{-2}$)
δ	thickness or depth (m)
ζ	thermal conductivity ($W\,m^{-1}\,K^{-1}$)
μ	number of moles of electrons participating in the reaction
ρ	density ($kg\,m^{-3}$)
ψ	wavelet function
Ψ	multi-dimensional wavelet function
Ω	ohmic resistance ($\Omega\,m^2$)

Superscripts

an	anode
c	cell unit
ca	cathode
e	electrochemical reaction
ls	lower separator
re	reforming reaction
sh	water–gas shift reaction
us	upper separator

under different operating conditions. In Ref. [12], a RBF neural network (NN) identification technology was employed to establish a dynamic model of a molten carbonate fuel cell (MCFC) stack that was used for designing a temperature controller. In Ref. [13], the Hammerstein nonlinear system, composed of a linear subsystem and a nonlinear subsystem, was applied to model the SOFC for dynamic response studies. The NN and Hammerstein model are both black-box modeling methods which are based on input and output data, and need not the priori knowledge about the internal structure of the object.

Among the black-box methods, the wavelet network is a novel and attractive modeling tool. The wavelet theory has been applied to many scientific areas such as signal processing and system identification [14,15]. The wavelet decomposition and multi-resolution approximation (MRA) guarantee that any function of $L^2(R)$ can be approximated to any prescribed accuracy with a finite sum of wavelets [14,15]. Wavelet networks combine the advantages of wavelets and neural networks, and provide an efficient constructive method for the implementation of networks [16]. Therefore, wavelet networks can be considered as an alternative to neural and radial basis function networks. Many researches [15–19] on the successful application of wavelet networks indicate that the approach is interesting and powerful. Combined with advanced control methods, wavelet networks can be used for controlling complicated coupling systems. Wai [19] successfully developed a robust controller with a wavelet network uncertainty observer to control the slider position of a motor-mechanism coupling system. Lin et al. [20] presented an adaptive wavelet network control system to control a synchronous motor servo drive system, and experimental results show an enhanced robust control performance.

In this paper, the aim is to identify a nonlinear black-box MIMO model for a DIR-SOFC stack using wavelet networks. The constructive process of the wavelet network mainly consists of three parts including generation of wavelet libraries, evolution of coefficients and selection of multi-dimensional wavelets used in the reconstruction of nonlinear functions. One of the advantages of the wavelet network is that it can be initialized according to the input and output data [16,17]. To implement the construction and optimization of the wavelet network, the recursive approach, the Gram–Schmidt algorithm, the Cross-Validation method and immune selection principles are employed.

The present study is organized into five sections. In Section 2, the physical model of the DIR-SOFC is described. In Section 3, the procedure for the wavelet network modeling is explained. In Section 4, nonlinear dynamic modeling of the DIR-SOFC stack using wavelet networks is detailedly described. Further, the modeling results and comparison of static and dynamic characteristics under different operating conditions are presented and discussed. Section 5 concludes the paper.

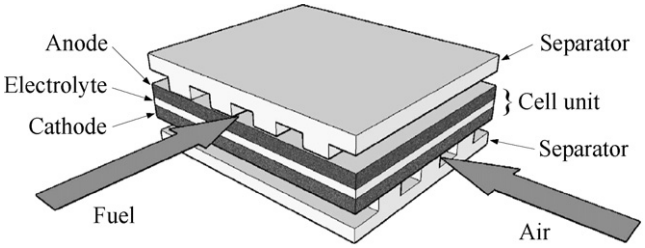

Fig. 1. Schematic diagram of a DIR-SOFC.

2. Physical model of DIR-SOFC

2.1. Reforming model

The layout of a DIR-SOFC is illustrated in Fig. 1. At the anode of the DIR-SOFC, the methane is reformed to hydrogen for oxidation in the electrochemical reaction [1,2]. The principal reactions in the methane steam-reforming are

$$CH_4 + 2H_2O \leftrightarrow CO_2 + 4H_2 \tag{1}$$

$$CH_4 + H_2O \leftrightarrow CO + 3H_2 \tag{2}$$

$$CO + H_2O \leftrightarrow CO_2 + H_2 \tag{3}$$

The reversible reactions obey the laws of chemical equilibrium. We denote by r_1, r_2 and r_3 the rates of reactions (1), (2) and (3), respectively. They are computed by

$$r_1 = \frac{(k_1/P_{H_2}^{3.5})(P_{CH_4}P_{H_2O}^2 - (P_{H_2}^4 P_{CO_2}/K_1))}{DEN^2}, \tag{4}$$

$$r_2 = \frac{(k_2/P_{H_2}^{2.5})(P_{CH_4}P_{H_2O} - (P_{H_2}^3 P_{CO}/K_2))}{DEN^2}, \tag{5}$$

$$r_3 = \frac{(k_3/P_{H_2})(P_{CO}P_{H_2O} - (P_{H_2}P_{CO_2}/K_3))}{DEN^2}. \tag{6}$$

DEN is defined as

$$DEN = \frac{1 + K_{CO}^{ad}P_{CO} + K_{H_2}^{ad}P_{H_2} + K_{CH_4}^{ad}P_{CH_4} + K_{H_2O}^{ad}P_{H_2O}}{P_{H_2}} \tag{7}$$

In Eqs. (4)–(7), P is the partial pressure; k_n, with $n = 1$–3, are the rate coefficients; K_n, with $n = 1$–3, are the equilibrium constants for the reforming reactions; K^{ad} the adsorption constants. k_n, K_n and K^{ad} are the functions of temperature which are presented in Ref. [21] detailedly. Reforming reaction rates are determined by the temperature, gas partial pressures, equilibrium constants, catalyst, etc. All these factors will be changed with the flows and reactions in the stack.

2.2. Electrochemical model

At the anode, the main electrochemical reaction is the oxidation of hydrogen [2]. At the cathode, molecular oxygen is reduced to negatively charged ions.

$$H_2 + O^{2-} \rightarrow H_2O + 2e^{2-} \tag{8}$$

$$(1/2)O_2 + 2e^- \rightarrow O^{2-} \tag{9}$$

The relation between the cell output voltage and the current density [4,9] is expressed as

$$V_{cell} = E - I\left(\Omega + \frac{RT^c}{\alpha^{an}F_{Far}I_0^{an}} + \frac{RT^c}{\alpha^{ca}F_{Far}I_0^{ca}}\right) + \frac{RT^c}{\mu F_{Far}}\ln\left(1 - \frac{I}{I_L}\right), \tag{10}$$

where I is the current density, Ω the ohmic resistance that depends on the material thickness and on the operating temperature, R the gas constant (8.314 J K^{-1} mol^{-1}), T^c the temperature of the cell unit, F_{Far} the Faraday constant (96,485 C mol^{-1}), α^{an} and α^{ca} are the charge transfer coefficients for the anode and cathode, respectively, μ is the number of moles of electrons participating in the reaction, and I_L is the limiting current density. The Nernst voltage of the cell, E, is calculated by

$$E = E_0 + \frac{RT^c}{2F_{Far}}\ln\left(\frac{P_{H_2}^{an}P_{O_2}^{ca\,1/2}}{P_{H_2O}^{an}}\right), \tag{11}$$

where E_0 is the EMF (electro-motive-force) at standard pressure [1].

Exchange current densities at the anode and cathode are respectively given by

$$I_0^{an} = \gamma^{an}\left(\frac{P_{H_2}^{an}}{P_{ref}}\right)\left(\frac{P_{H_2O}^{an}}{P_{ref}}\right)\exp\left(-\frac{E_{act}^{an}}{RT^c}\right), \tag{12}$$

$$I_0^{ca} = \gamma^{ca}\left(\frac{P_{O_2}^{ca}}{P_{ref}}\right)^{0.25}\exp\left(-\frac{E_{act}^{ca}}{RT^c}\right), \tag{13}$$

where γ^{an} and γ^{ca} are coefficients, E_{act}^{an} and E_{act}^{ca} are the activation energies, and P_{ref} is the reference pressure (1 bar) [4].

The electrochemical reaction rates are directly related to the current density. The rates of reactions (8) and (9) (r_4 and r_5) are calculated by

$$r_4 = r_5 = \frac{I}{2F_{Far}}. \tag{14}$$

2.3. Thermal model

Reforming reactions are highly endothermic reactions. The electrochemical reaction is exothermic and supplies heat and steam to the endothermic reforming reactions. Non-uniform reaction rate distribution in the stack makes the differences of released heat across the stack, and the heat is transferred between each component of the fuel cells (including convection, radiation and conduction).

For the fuel and air flows, the energy equation is given as

$$\frac{\partial(\rho h)}{\partial t} + \mathrm{div}\left(\rho h\vec{V} - \frac{\zeta\nabla h}{C_p}\right) = S_h, \tag{15}$$

where ρ is the density, h the gas enthalpy, $\vec{V}$ the gas velocity vector, ζ the thermal conductivity, div denotes the divergence, ∇ denotes the gradient, C_p the specific heat capacity and S_h is the heat source.

For the cell unit and the separators, the energy equation can be simplified as

$$\rho C_p \frac{\partial T}{\partial t} - \mathrm{div}(\zeta \nabla T) = S_\mathrm{h}. \tag{16}$$

The local heat released by electrochemical reactions is expressed by

$$q^\mathrm{e} = -\Delta H^\mathrm{e} r_4 - V_\mathrm{cell} I, \tag{17}$$

where $V_\mathrm{cell}I$ is the local output electrical power produced by the SOFC.

The heat changes caused by reforming reactions and the water–gas shift reaction are respectively given by

$$q^\mathrm{re} = -\Delta H_1 r_1 - \Delta H_2 r_2, \tag{18}$$

$$q^\mathrm{sh} = -\Delta H_3 r_3. \tag{19}$$

Besides the heat generation, the convective and radiant heat transfers between the cell unit, separators and flows are taken into account. For each object, S_h in Eqs. (15) and (16) will be given differently.

cell unit:

$$S_\mathrm{h}^\mathrm{c} = \frac{q^\mathrm{e} + q^\mathrm{re}}{\delta^\mathrm{c}} \tag{20}$$

separators:

$$S_\mathrm{h}^\mathrm{us} = S_\mathrm{h}^\mathrm{ls} = 0 \tag{21}$$

fuel flow:

$$S_\mathrm{h}^\mathrm{fuel} = \frac{q^\mathrm{sh}}{\delta^\mathrm{fuel}} \tag{22}$$

air flow:

$$S_\mathrm{h}^\mathrm{air} = 0 \tag{23}$$

In Eqs. (20) and (22), δ^c and δ^fuel are the cell unit thickness and the fuel channel depth, respectively.

2.4. Mass conservation

The continuous reforming and electrochemical reactions change the chemical species concentrations in the flows, when the fuel and air pass over the electrodes of the SOFC. Since all gases are assumed to be ideal gases, the gas flow rates are expressed by

$$\begin{bmatrix} F^\mathrm{fuel} \\ F^\mathrm{air} \end{bmatrix} = \begin{bmatrix} F_0^\mathrm{fuel} \\ F_0^\mathrm{air} \end{bmatrix} + \begin{bmatrix} \vec{W}_1 \iint_{A_1} B_1 \vec{r}\, \mathrm{d}A_1 \\ \vec{W}_2 \iint_{A_2} B_2 r_5\, \mathrm{d}A_2 \end{bmatrix}, \tag{24}$$

where F_0 is the inlet gas flow rate, A_1 and A_2 are anodic and cathodic reaction surfaces, respectively. $\vec{W}_1$ and $\vec{W}_2$ are the molar mass vectors of the fuel and air, respectively. Stoichiometric matrices B_1 and B_2, and reaction rate vector $\vec{r}$ are respectively given by

$$B_1 = \begin{bmatrix} -1 & -1 & 0 & 0 \\ 1 & 0 & 1 & 0 \\ 0 & 1 & -1 & 0 \\ 4 & 3 & 1 & -1 \\ -2 & -1 & -1 & 1 \end{bmatrix}, \tag{25}$$

$$B_2 = \begin{bmatrix} -1/2 \\ 0 \end{bmatrix}, \tag{26}$$

$$\vec{r} = (r_1, r_2, r_3, r_4)^\mathrm{T}. \tag{27}$$

3. Wavelet network modeling

3.1. Wavelet decomposition

A function $\psi(x) \in L^2(R)$ is admissible as a wavelet, if its Fourier transform $\hat{\psi}(\omega)$ satisfies

$$C_\psi = \int_0^\infty \frac{|\hat{\psi}(\omega)|^2}{\omega} \mathrm{d}\omega < \infty. \tag{28}$$

For any function $f(x) \in L^2(R)$, its continuous wavelet transform is defined as

$$w(a, b) = \int_R f(x) \overline{\psi_{a,b}(x)}\, \mathrm{d}x, \tag{29}$$

where $a \in R_+$ and $b \in R$ are dilation and translation parameters, respectively [14,15]. $\psi_{a,b}(x)$ is obtained by scaling mother wavelet $\psi(x)$ by a and translating it by b:

$$\psi_{a,b}(x) = a^{-1/2} \psi\left(\frac{x - b}{a}\right). \tag{30}$$

The function $f(x)$ can be reconstructed by the inverse wavelet transform

$$f(x) = C_\psi^{-1} \int_0^\infty \int_{-\infty}^\infty w(a, b) \psi_{a,b}(x) \frac{\mathrm{d}a}{a^2}\, \mathrm{d}b. \tag{31}$$

As a matter of fact, the continuous wavelet transform and its inverse transform need to be implemented on digital computers. The reconstruction equation is thus discretized into

$$f(x) = \sum_l w_l \psi_l(x), \tag{32}$$

where

$$\psi_l(x) = a_0^{m/2} \psi(a_0^m x - n b_0), \tag{33}$$

and l represents the integer pair (m, n).

For multivariable nonlinear coupling systems, we construct multi-dimensional wavelets Ψ by using the product of N_input (the number of input variables) scalar wavelets.

$$\Psi_l(\vec{x}) = \prod_{i=1}^{N_\mathrm{input}} \psi\left(\frac{x_i - b_{li}}{a_{li}}\right), \tag{34}$$

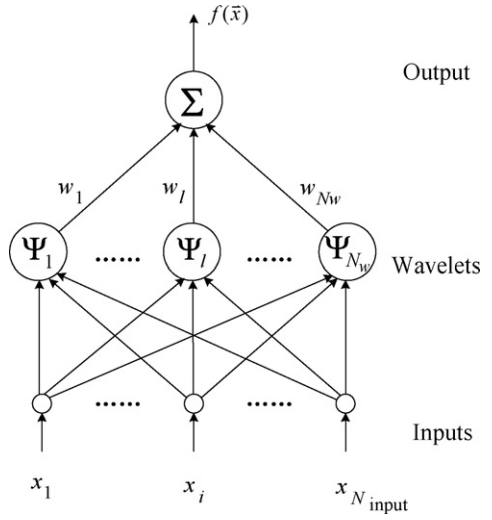

Fig. 2. Diagram of the multi-dimensional wavelet reconstruction.

where

$$a_{li} = a_0^{-m_i}, \tag{35}$$

$$b_{li} = n_i a_0^{-m_i} b_0, \tag{36}$$

$$\vec{x} = (x_1, \ldots, x_i, \ldots, x_{N_{\text{input}}})^{\text{T}}. \tag{37}$$

The reconstruction of the multivariable function can be written as

$$f(\vec{x}) = \sum_{l}^{N_{\text{w}}} w_l \Psi_l(\vec{x}). \tag{38}$$

The multi-dimensional wavelet decomposition of $f(\vec{x})$ can be regarded as a one-hidden-layer network (shown in Fig. 2) with Ψ as the activation function of the hidden neurons and with the coefficient w_l as the weight of the hidden layer.

3.2. Initialization of wavelet networks

Using MRA of the wavelet transform, it can be shown that the bigger N_{w} (the number of multi-dimensional wavelets used in reconstruction) and wider ranges of dilation and translation parameters would result in a better approximation of the function [14,15]. In practice, however, the multi-dimensional available data are finite and sparse. Many dilated and translated wavelets do not contain any data point in their supports and actually have no contribution to the function reconstruction [16]. They will not improve the approximation accuracy, but increase the computational time and the storage requirements. Therefore, generating wavelet libraries and eliminating the redundant wavelets are beneficial and necessary.

3.2.1. Generating wavelet libraries

Discrete dyadic wavelets ($a_0 = 2$, $b_0 = 1$) are the typical biorthogonal wavelet bases. We generate the libraries according to the distribution of the available training data, and select the scalar wavelets from the libraries to construct the multi-dimensional wavelets. We denote by $[\min_i, \max_i]$ the domain containing the values of the ith component of the input vectors. In order to guarantee that the wavelets extend initially over the whole domain of the ith component of the input vectors, relations (39) and (40) should be satisfied [17].

$$2^{-m_i} \le \theta(\max_i - \min_i), \tag{39}$$

and

$$\min_i \le 2^{-m_i} n_i \le \max_i, \tag{40}$$

where θ is a parameter adjusted according to the mother wavelet.

Hence, we can obtain

$$m_i \ge -\log_2(\theta(\max_i - \min_i)), \tag{41}$$

and

$$2^{m_i} \min_i \le n_i \le 2^{m_i} \max_i. \tag{42}$$

Under above two conditions (relations (41) and (42)), we generate two integer sets

$$S_{m_i} = \{\lceil -\log_2(\theta(\max_i - \min_i))\rceil,\ \lceil -\log_2(\theta(\max_i - \min_i))\rceil + 1,\ \lceil -\log_2(\theta(\max_i - \min_i))\rceil + 2,\ \lceil -\log_2(\theta(\max_i - \min_i))\rceil + 3\}, \tag{43}$$

and

$$S_{n_i} = \{\lceil 2^{m_i}\min_i\rceil,\ \lceil 2^{m_i}\min_i\rceil + 1,\ \ldots,\ \lfloor 2^{m_i}\max_i\rfloor\}, \tag{44}$$

where $\lceil\ \rceil$ represents rounding toward ceiling, and $\lfloor\ \rfloor$ represents rounding toward floor.

S_{m_i} and S_{n_i} are the dilation and translation sets, respectively. As can be seen from Eq. (44), the translations depend on the values of dilations; the number of translations increases exponentially with m_i. We denote by $\{S_{m_i}, S_{n_i}\}$ the wavelet library for the ith component of the input vectors. The wavelet library for all N_{input} input components is $\bigcup_{i=1}^{N_{\text{input}}}\{S_{m_i}, S_{n_i}\}$.

3.2.2. Selection of wavelets

From all the possible combinations of scalar wavelets, we select a number of combinations, which contain most useful information, to construct the wavelet network. In Section 3.2.1, the wavelet libraries are generated based on the input data, not on the output data. To eliminate the redundant wavelets in the libraries for the estimation of f, we employ the Gram–Schmidt algorithm relying on the input and output data.

The Gram–Schmidt algorithm is a recursive process which aims to obtain an orthogonal basis from a non-orthogonal set [22]. It first selects a multi-dimensional wavelet from the libraries that best fits the training data as the initial basis, and then repeatedly selects the multi-dimensional wavelets in the remainder to enlarge the basis so that the basis can best fit the data. The reader is referred to [22] for the details of the Gram–Schmidt algorithm.

Assume that we obtain N_{w} multi-dimensional wavelets by Gram–Schmidt algorithm as follows

$$\{\Psi_1, \ldots, \Psi_l, \ldots \Psi_{N_{\text{w}}}\}. \tag{45}$$

The hidden layer of the network is made up of the selected wavelets. The determination of N_w will be given in Section 3.3.2.

3.3. Training algorithm

3.3.1. Coefficients of wavelets

The MIMO system can be considered as the synthesis of several MISO subsystems. Thus, we can separately train each MISO subsystem. Considering a training data set $\{(\vec{x}(k), y(k))|k = 1, \ldots, N_t\}$ generated by a system with N_{input} inputs and a scalar output, we use the recursive method to update the coefficients.

Iterative updating formulas for $w_{l_s}(k)$, which is the coefficient of $\Psi_{l_s}(\vec{x}(k))$ at iteration k, are given as follows:

$$e(k) = y(k) - \sum_{l=1}^{N_w} w_l(k-1)\Psi_l(\vec{x}(k)), \tag{46}$$

$$d_{l_s}(k) = \lambda d_{l_s}(k-1) + \Psi_{l_s}^2(\vec{x}(k)), \tag{47}$$

$$w_{l_s}(k) = w_{l_s}(k-1) + \frac{\Psi_{l_s}(\vec{x}(k))e(k)}{d_{l_s}(k)}. \tag{48}$$

In Eq. (47), $0 < \lambda \leq 1$ is the forgetting factor that indicates the different importance of data. The data near iteration k are more important than those far away [23]. The derivation of Eqs. (46)–(48) is presented in Appendix A. Updating recursions for coefficients of other wavelets are similar to Eqs. (46)–(48).

3.3.2. Number of multi-dimensional wavelets

In Section 3.2.2, we assume the number of multi-dimensional wavelets in the network is N_w, and select the wavelets by Gram–Schmidt algorithm. However, choosing the number N_w is a difficult process. The wavelet network model is expected to have relatively high accuracy when evaluated not only with training data but also with fresh data. If N_w is over large, the wavelet network will be too complex and tend to overfit the training data. On the other hand, a wavelet network that is not sufficiently complex (over small N_w) can fail to detect fully the signal in a complicated data set, leading to underfitting [16,24].

For this reason, the Cross-Validation method is employed to estimate N_w. The available data are divided into two parts when training the model. One part is used for estimating the model parameters. The quality of performances of the model on the other part of the data reflects how well it would perform in an unsupervised setting. The Cross-Validation criterion is given by

$$\mathrm{CV} = \frac{1}{N_t'}\sum_{k=1}^{N_t'}(\hat{f}_{N_w}(\vec{x}(k)) - y(k))^2, \tag{49}$$

where $\hat{f}_{N_w}$ is the trained wavelet network with N_w multi-dimensional wavelets. The data set $\{(\vec{x}(k), y(k))|k = 1, \ldots, N_t'\}$ used in Eq. (49) is different from the training data set. Hence, N_w is determined by minimizing CV.

The modeling procedures of wavelet networks can be summarized as a flowchart in Fig. 3.

In the flowchart, N_w should be repeatedly selected until $\mathrm{CV} < \varepsilon_{CV}$. Several selection approaches exit. The immune algorithm is a heuristically random searching algorithm which is developed as an imitation of the adaptive humoral immune response [25]. It has been proved to be capable of performing such tough tasks as machine learning and quadratic optimization. In this paper, we use immune algorithm for selecting N_w so that the Cross-Validation criterion is gradually decreased after selections.

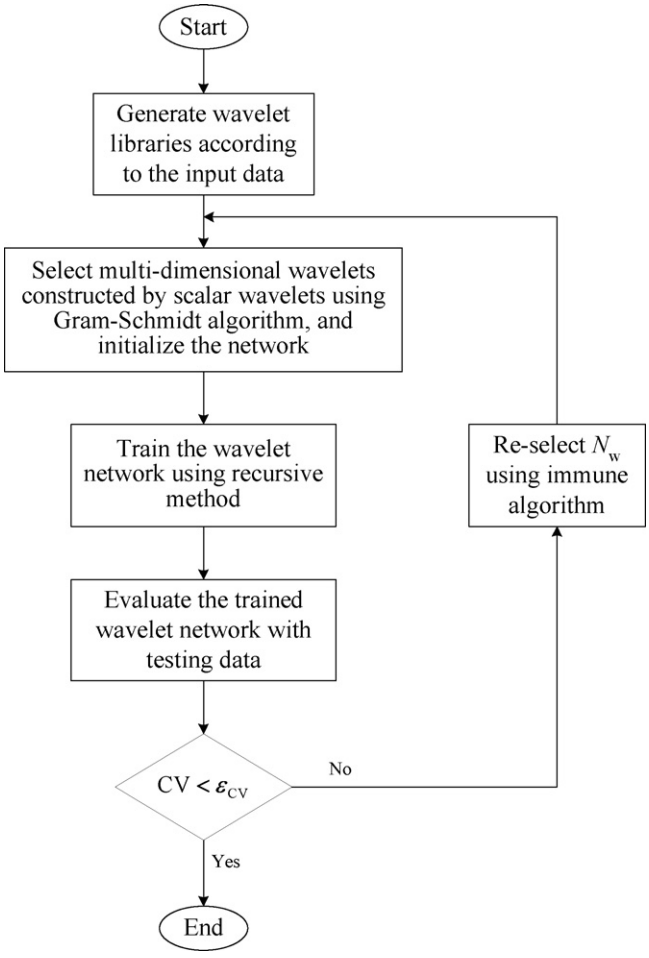

Fig. 3. Flowchart of the wavelet network modeling approach.

4. Results

Many factors such as flow rates, temperature, pressure, material and configuration can influence the operating performance of the DIR-SOFC. Furthermore, the nonlinear coupling variables and parameters can increase difficulty in analyzing the operating states of the DIR-SOFC. For a black-box model, we need not consider all the factors, and can concentrate on the important variables and parameters which we are interested in. The current density–voltage characteristic is important for fuel cells; and the thermodynamic performance of the stack is also crucial for designing and controlling the DIR-SOFC.

The DIR-SOFC can be regarded as a system with three-input (F_0^{fuel}, F_0^{air} and V_{out}) and two-output (T_{out} and I_m). V_{out}, T_{out} and I_m are the stack output voltage, the outlet temperature and the mean current density, respectively. We assume that the DIR-

SOFC can be modeled by equations of the following form.

$$T_{\text{out}}(k) = f_1(V_{\text{out}}(k-1),\ V_{\text{out}}(k-2),\ \vec{F}(k-1),\ \vec{F}(k-2),\ T_{\text{out}}(k-1),\ T_{\text{out}}(k-2)), \tag{50}$$

$$I_{\text{m}}(k) = f_2(V_{\text{out}}(k-1),\ V_{\text{out}}(k-2),\ \vec{F}(k-1),\ \vec{F}(k-2),\ I_{\text{m}}(k-1),\ I_{\text{m}}(k-2)), \tag{51}$$

where f_1 and f_2 are unknown nonlinear functions, and $\vec{F}$ represents $(F_0^{\text{fuel}}, F_0^{\text{air}})^{\text{T}}$. We expect to estimate functions f_1 and f_2 so that the behavior of model is close to that of the real DIR-SOFC stack. In order to fit into the framework of the wavelet network as formulated in Section 3, let

$$\{\vec{x} = (V_{\text{out}}(k-1),\ V_{\text{out}}(k-2),\ \vec{F}(k-1),\ \vec{F}(k-2),\ T_{\text{out}}(k-1),\ T_{\text{out}}(k-2))^{\text{T}},\quad y = T_{\text{out}}(k)\} \tag{52}$$

and

$$\{\vec{x} = (V_{\text{out}}(k-1),\ V_{\text{out}}(k-2),\ \vec{F}(k-1),\ \vec{F}(k-2),\ I_{\text{m}}(k-1),\ I_{\text{m}}(k-2))^{\text{T}},\quad y = I_{\text{m}}(k)\}. \tag{53}$$

In our study, the mother wavelet has been chosen as

$$\psi(x) = -x \exp\left(-\frac{1}{2}x^2\right), \tag{54}$$

and θ as 0.2. The wavelet network modeling of the DIR-SOFC is implemented based on simulation data.

4.1. Preparing simulation data

The system under consideration is a 16 kW DIR-SOFC stack that consists of 30 cells operating in cross-flow mode. The dynamic physical model of the DIR-SOFC stack is developed in MATLAB to generate simulation data. The schematic illustration of the physical model of one cell is shown in Fig. 4. The cell is divided into several elements which are mutually connected by bidirectional arrows. The fuel and air are respectively injected into the cell in orthogonal directions and pass sequentially through one element to the next element. The interaction (temperature, gas flows, etc.) between adjacent elements is taken into account and is indicated by bidirectional arrows in Fig. 4.

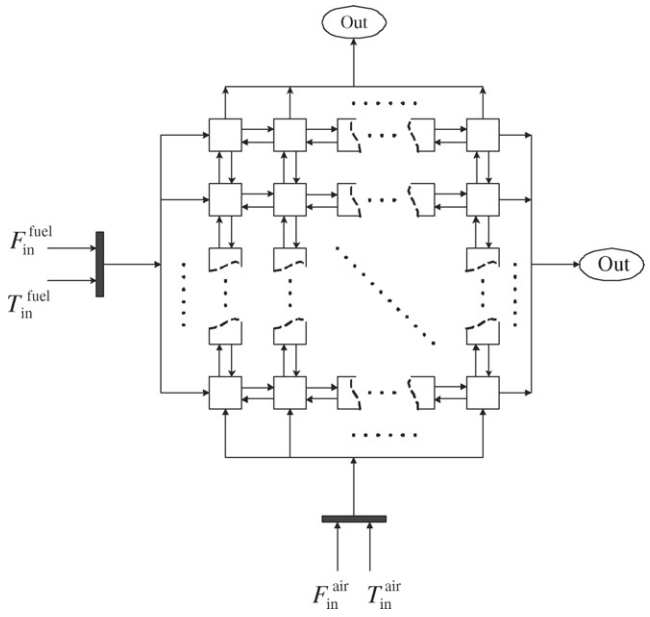

Fig. 4. Schematic illustration of the physical model of one cell.

Fig. 5 illustrates the implementation of the element in MATLAB/Simulink. The element module is composed of the reforming module, electrochemical module and temperature module. We write S-functions in C language and generate masked S-function blocks that can be invoked as sub-modules. In

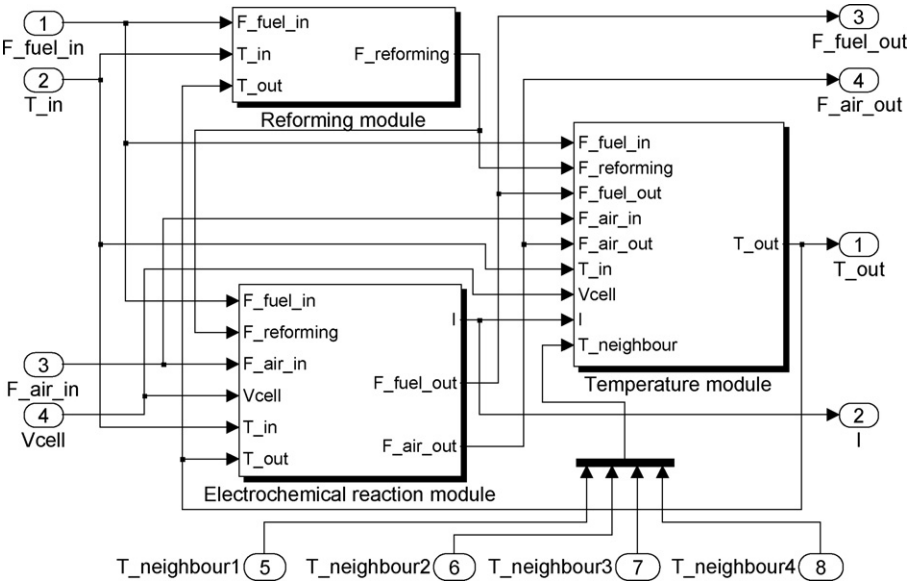

Fig. 5. Implementation of the element in MATLAB/Simulink.

Table 1
Operating conditions and parameters of the DIR-SOFC stack

Item	Value	Unit
Number of cell	30	
Cell area	0.16	m^2
Power	16	kW
Mean current density	100–8900	$A\,m^{-2}$
Output voltage	8–28	V
Fuel flow rate	0.5–3	$10^{-3}\,kg\,s^{-1}$
Air flow rate	0.7–3	$10^{-2}\,kg\,s^{-1}$
Inlet fuel temperature	980–1320	K
Inlet air temperature	980–1320	K
Inlet composition of fuel		
CH_4	28%	mol/mol
CO_2	1%	mol/mol
CO	1%	mol/mol
H_2	10%	mol/mol
H_2O	60%	mol/mol
Inlet composition of air		
O_2	23.7%	mol/mol
N_2	76.3%	mol/mol
Operating pressure	3	bar
Anodic activation energy	1.2×10^5	$J\,mol^{-1}$
Cathodic activation energy	1.2×10^5	$J\,mol^{-1}$
γ^{an}	2.9×10^8	$A\,m^{-2}$
γ^{ca}	7×10^8	$A\,m^{-2}$
Limiting current density	9000	$A\,m^{-2}$

Fig. 5, $T_{\text{-in}}$, $T_{\text{-out}}$ and $T_{\text{-neighbour}}$ are vectors whose components are temperatures of the cell unit, fuel, air and separators. $T_{\text{-in}}$ and $T_{\text{-out}}$ denote the inlet and outlet temperature vectors of the element, respectively. Four $T_{\text{-neighbour}}$ represent the temperature information of the adjacent elements.

The variables and parameters of the dynamic physical model are listed in Table 1. The dynamic physical model is excited with the fuel flow rate ($(0.5–3) \times 10^{-3}\,kg\,s^{-1}$), the air flow rate ($(0.7–3) \times 10^{-2}\,kg\,s^{-1}$), inlet temperature (980–1320 K) and the output voltage (8–28 V) to generate data. 16,000 data are obtained from the simulation and are split into two parts. One part (8000 data) is used for the construction and identification of the wavelet networks, and the other part (8000 data) is used for the evaluation of the resulting wavelet networks.

4.2. Predicting with wavelet networks

Using the approaches described in Section 3, wavelet networks are thus constructed based on the first part of data. The identification results of the numbers of multi-dimensional wavelets used in the networks, N_w, are 32 for f_1 and 35 for f_2 (corresponding to $\varepsilon_{CV} = 0.3$), respectively.

Fig. 6 shows the comparison of V_{out}–I_m characteristics generated by the resulting wavelet networks and the physical model. We can see that the static V_{out}–I_m characteristics predicted by the wavelet networks show good consistency with the physical model under various temperature.

For controlling the DIR-SOFC stack, the dynamic predictive capability of the model is more important. Two cases are used as examples to evaluate the dynamic performance of the obtained wavelet networks.

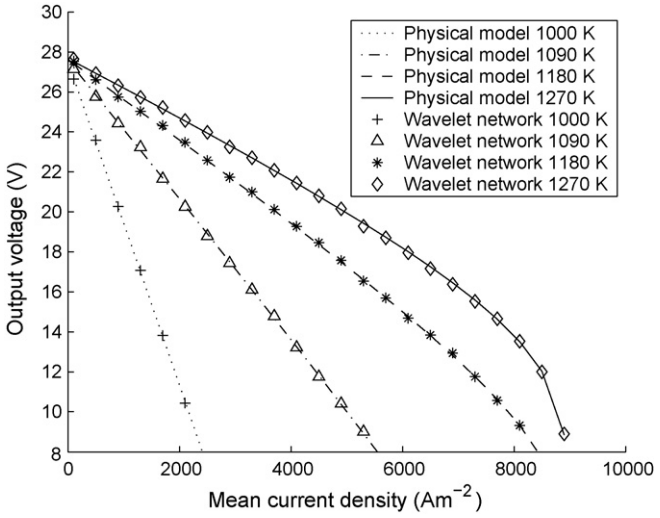

Fig. 6. Comparison of V_{out}–I_m characteristics.

(1) Fuel flow rate increases from 8.21×10^{-4} to $9.43 \times 10^{-4}\,kg\,s^{-1}$, and air flow rate maintains $1.24 \times 10^{-2}\,kg\,s^{-1}$;
(2) air flow rate decreases from 1.24×10^{-2} to $1.12 \times 10^{-2}\,kg\,s^{-1}$, and fuel flow rate maintains $8.21 \times 10^{-4}\,kg\,s^{-1}$.

In these two cases, the inlet temperature (1024 K), the stack output voltage (21 V) and operating pressure (3 bar) are kept constant.

The comparison of dynamic responses of the wavelet networks and the physical model is shown in Figs. 7–10. Figs. 7 and 8 present the responses of outlet temperature and mean current density for Case 1, Figs. 9 and 10 for Case 2.

In Case 1, the magnitude of changes in outlet temperature and mean current density are relatively large, and the curves generated by the wavelet networks and the physical model are too close to distinguish. For a closer look of the results, zooms

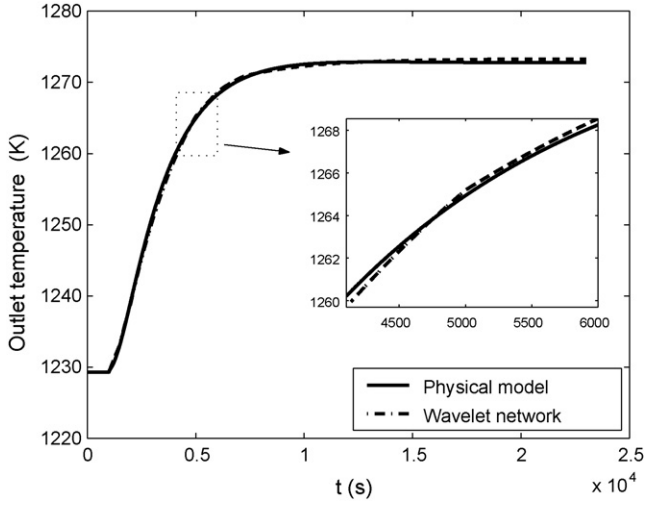

Fig. 7. Dynamic response of outlet temperature for Case 1.

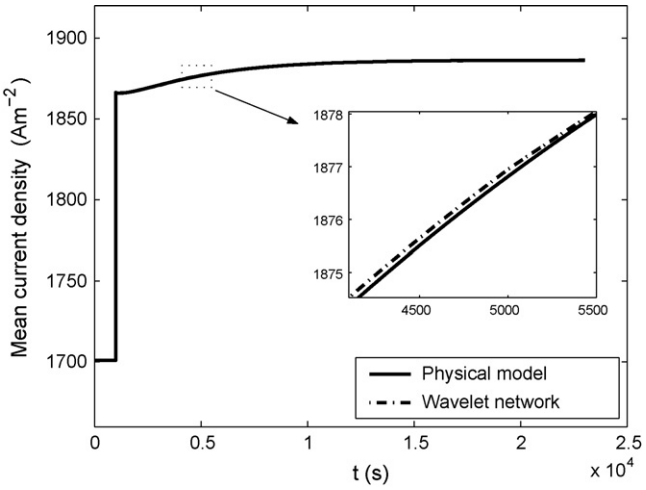

Fig. 8. Dynamic response of mean current density for Case 1.

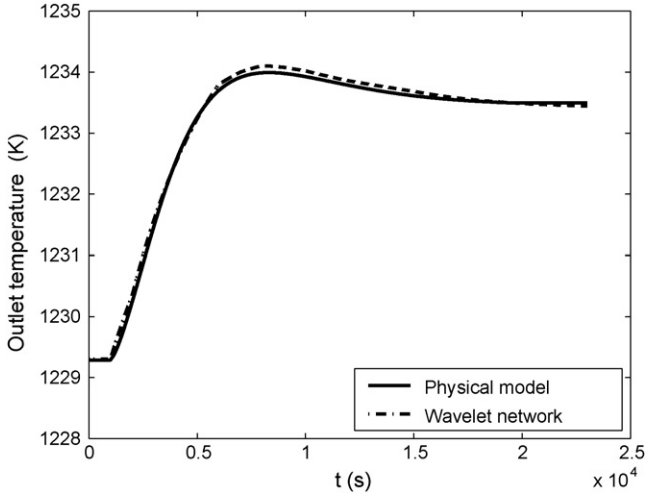

Fig. 9. Dynamic response of outlet temperature for Case 2.

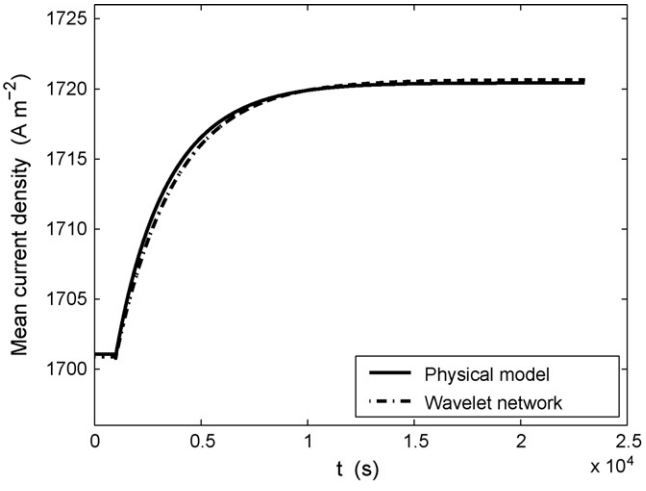

Fig. 10. Dynamic response of mean current density for Case 2.

Table 2
Statistical results for two cases

Case	Outlet temperature		Mean current density	
	MSE	CC	MSE	CC
1	0.1212	0.9997	0.2106	0.9993
2	0.0054	0.9992	0.1189	0.9989

Table 3
Computational time for two cases

Case	Computational time (s)			
	Outlet temperature		Mean current density	
	Physical model	Wavelet network	Physical model	Wavelet network
1	3.39975053×10^5	0.916	3.39975053×10^5	0.928
2	3.23977547×10^5	0.872	3.23977547×10^5	0.907

of the curves are inset in corresponding figures (Figs. 7 and 8). The mean squared errors (MSE) and the correlation coefficients (CC) between the wavelet network output and the physical model output in two cases are computed and presented in Table 2. As can be seen from Figs. 7–10 and Table 2, the proposed method is successful in identifying the DIR-SOFC dynamics.

5. Conclusions

Nonlinear identification of a DIR-SOFC stack using wavelet networks is described in this paper. Combining the MRA of wavelets and evolution of networks, the wavelet network approach is classified as black-box modeling, and avoids using complicated multiple partial differential equations of energy balance and mass conservation. The simulation programs operate on a Pentium 4 2.80 GHz computer with 256 MB memory. Table 3 shows the comparison of computational time (required for the response curve to reach a steady-state) between the physical model and wavelet networks for different cases (increasing the fuel flow rate and decreasing the air flow rate). As can be seen from Table 3, the computational time for calculating the response curve by using wavelet networks is less than 1 s, and is much shorter than the computational time needed by the physical model. Simulation results illustrate fast and robust adaptation of the wavelet network model following changes in operating conditions. The static and dynamic characteristics of the DIR-SOFC stack can be predicted with relatively high accuracy. It is shown that the presented wavelet network is a powerful and attractive method for the identification of a DIR-SOFC stack. The obtained wavelet network model can facilitate analysis of system stability and be used for designing model-based controllers. In the future, the model is planned to be used for developing predictive and robust controllers for the DIR-SOFC stack.

Acknowledgement

This work is supported by the Hi-Tech Research and Development Program (863) of China (No. 2006AA05Z148).

Appendix A. Derivation of iterative updating formulas

Assume that, at iteration k, the estimation of w_{l_s} corresponding to $\Psi_{l_s}(\vec{x}(k))$ is $\hat{w}_{l_s}$, while the coefficients of other multi-dimensional wavelets are $w_l(k-1)\,(l \neq l_s)$. We define

$$\tilde{y}(k) = \sum_{l \neq l_s}^{N_w} w_l(k-1)\Psi_l(\vec{x}(k)) + \hat{w}_{l_s}\Psi_{l_s}(\vec{x}(k)). \tag{A.1}$$

A least squares cost function with forgetting factor is defined as

$$\varepsilon(k) = \sum_{j=1}^{k} (y(j) - \tilde{y}(j))^2 \lambda^{k-j}, \tag{A.2}$$

where $0 < \lambda \leq 1$ is the forgetting factor [23]. $w_{l_s}(k)$ is estimated by minimizing $\varepsilon(k)$ (Eq. (A.2)). The partial derivative of the cost function with respect to $\hat{w}_{l_s}$ is

$$\begin{aligned}
\frac{\partial \varepsilon(k)}{\partial \hat{w}_{l_s}} &= -2\sum_{j=1}^{k} (y(j) - \tilde{y}(j)) \frac{\partial \tilde{y}(j)}{\partial \hat{w}_{l_s}} \lambda^{k-j} \\
&= -2\sum_{j=1}^{k} (y(j) - \tilde{y}(j)) \Psi_{l_s}(\vec{x}(j)) \lambda^{k-j} \\
&= -2\sum_{j=1}^{k} \left(y(j) - \sum_{l \neq l_s}^{N_w} w_l(j-1)\Psi_l(\vec{x}(j)) - \hat{w}_{l_s}\Psi_{l_s}(\vec{x}(j)) \right) \\
&\quad \Psi_{l_s}(\vec{x}(j)) \lambda^{k-j}
\end{aligned} \tag{A.3}$$

Let

$$\frac{\partial \varepsilon(k)}{\partial \hat{w}_{l_s}} = 0 \tag{A.4}$$

Hence,

$$\begin{aligned}
w_{l_s}(k) &= \hat{w}_{l_s} \\
&= \frac{\sum_{j=1}^{k} \left(y(j) - \sum_{l \neq l_s}^{N_w} w_l(j-1)\Psi_l(\vec{x}(j)) \right) \Psi_{l_s}(\vec{x}(j)) \lambda^{k-j}}{\sum_{j=1}^{k} \Psi_{l_s}^2(\vec{x}(j)) \lambda^{k-j}}.
\end{aligned} \tag{A.5}$$

Let

$$d_{l_s}(k) = \sum_{j=1}^{k} \Psi_{l_s}^2(\vec{x}(j)) \lambda^{k-j}. \tag{A.6}$$

Rewriting Eqs. (A.5) and (A.6) as recursions:

$$e(k) = y(k) - \sum_{l=1}^{N_w} w_l(k-1)\Psi_l(\vec{x}(k)), \tag{A.7}$$

$$d_{l_s}(k) = \lambda d_{l_s}(k-1) + \Psi_{l_s}^2(\vec{x}(k)), \tag{A.8}$$

$$w_{l_s}(k) = w_{l_s}(k-1) + \frac{\Psi_{l_s}(\vec{x}(k))e(k)}{d_{l_s}(k)}. \tag{A.9}$$

Eqs. (A.7)–(A.9) are used for updating w_{l_s}.

References

[1] J. Larminie, A. Dicks, Fuel Cell Systems Explained, Wiley, New York, 2000.
[2] P. Vernoux, J. Guindet, M. Kleitz, Gradual internal methane reforming in intermediate-temperature solid-oxide fuel cells, J. Electrochem. Soc. 145 (10) (1998) 3487–3492.
[3] E. Achenbach, Three-dimensional and time-dependent simulation of a planar solid oxide fuel cell stack, J. Power Sources 49 (1–3) (1994) 333–348.
[4] P. Costamagna, K. Honegger, Modeling of solid oxide heat exchanger integrated stacks and simulation at high fuel utilization, J. Electrochem. Soc. 145 (11) (1998) 3995–4007.
[5] J. Padulles, G.W. Ault, J.R. McDonald, An integrated SOFC plant dynamic model for power systems simulation, J. Power Sources 86 (1/2) (2000) 495–500.
[6] J. Palsson, A. Selimovic, L. Sjunnesson, Combined solid oxide fuel cell and gas turbine systems for efficient power and heat generation, J. Power Sources 86 (1/2) (2000) 442–448.
[7] A. Selimovic, J. Palsson, Networked solid oxide fuel cell stacks combined with a gas turbine cycle, J. Power Sources 106 (1–2) (2002) 76–82.
[8] K.P. Recknagle, R.E. Williford, L.A. Chick, D.R. Rector, M.A. Khaleel, Three-dimensional thermo-fluid electrochemical modeling of planar SOFC stacks, J. Power Sources 113 (1) (2003) 109–114.
[9] P. Aguiar, C.S. Adjiman, N.P. Brandon, Anode-supported intermediate temperature direct internal reforming solid oxide fuel cell. I. Model-based steady-state performance, J. Power Sources 138 (1/2) (2004) 120–136.
[10] P. Aguiar, C.S. Adjiman, N.P. Brandon, Anode-supported intermediate-temperature direct internal reforming solid oxide fuel cell: II. Model-based dynamic performance and control, J. Power Sources 147 (1/2) (2005) 136–147.
[11] J. Arriagada, P. Olausson, A. Selimovic, Artificial neural network simulator for SOFC performance prediction, J. Power Sources 112 (1) (2002) 54–60.
[12] C. Shen, G.-Y. Cao, X.-J. Zhu, X.-J. Sun, Nonlinear modeling and adaptive fuzzy control of MCFC stack, J. Process Contr. 12 (8) (2002) 831–839.
[13] F. Jurado, A method for the identification of solid oxide fuel cells using a Hammerstein model, J. Power Sources 154 (1) (2006) 145–152.
[14] C.K. Chui, An Introduction to Wavelets, Academic Press, New York, 1992.
[15] S. Mallat, A Wavelet Tour of Signal Processing, second ed., Academic Press, San Diego, 1999.
[16] Q. Zhang, A. Benveniste, Wavelet networks, IEEE Trans. Neural Netw. 3 (6) (1992) 889–898.
[17] Y. Oussar, I. Rivals, L. Personnaz, G. Dreyfus, Training wavelet networks for nonlinear dynamic input-output modeling, Neurocomputing 20 (1–3) (1998) 173–188.
[18] C.-H. Lin, C.-H. Wang, Adaptive wavelet networks for power-quality detection and discrimination in a power system, IEEE Trans. Power Deliv. 21 (3) (2006) 1106–1113.
[19] R.-J. Wai, Robust control for nonlinear motor-mechanism coupling system using wavelet neural network, IEEE Trans. Syst. Man Cybern. Part B-Cybern. 33 (3) (2003) 489–497.
[20] F.-J. Lin, P.-H. Shen, Y.-S. Kung, Adaptive wavelet neural network control for linear synchronous motor servo drive, IEEE Trans. Magn. 41 (12) (2005) 4401–4412.
[21] J. Xu, G.F. Froment, Methane steam reforming, methanation and water–gas shift: I. Intrinsic kinetics, AIChE J. 35 (1) (1989) 88–96.
[22] G.B. Arfken, H.J. Weber, Mathematical Methods for Physicists, fifth ed., Harcourt/Academic Press, San Diego, 2001.
[23] Y. Zhu, Efficient recursive state estimator for dynamic systems without knowledge of noise covariances, IEEE Trans. Aerosp. Electron. Syst. 35 (1) (1999) 102–114.
[24] T.Q. Huynh, R. Setiono, Effective neural network pruning using cross-validation, in: Proceedings of 2005 IEEE International Joint Conference on Neural Networks, Montreal, Canada, 2005, pp. 972–977.
[25] L.N. de Castro, F.J. Von Zuben, Learning and optimization using the clonal selection principle, IEEE Trans. Evol. Comput. 6 (3) (2002) 239–251.